



Enhancing photocatalytic CO₂ reduction reaction on amorphous Ni@NiO aerogel via oxygen incorporated tuning

Zuqi Zhong ^a, Haofan Wang ^a, Shujie Liang ^{a,*}, Xiaohui Zhong ^a, Hong Deng ^{a,b, **}

^a School of Environment and Energy, Guangdong Provincial Key Laboratory of Solid Wastes Pollution Control and Recycling, The Key Laboratory of Pollution Control and

Ecosystem Restoration in Industry Clusters (Ministry of Education), South China University of Technology, Guangzhou, Guangdong 510006, China

^b Guangdong Engineering and Technology Research Center for Environmental Nanomaterials, South China University of Technology, Guangzhou, Guangdong 510006, China



ARTICLE INFO

Keywords:

Non-noble metal photocatalyst
CO₂ photoreduction
Metal aerogel

ABSTRACT

Photochemical CO₂ reduction to CO, acting as a mild and feasible method, holds huge prospects for atmospheric CO₂ level diminution. Non-noble metal aerogel has been supposed to be an appealing material in the field of catalysis, yet suffering from low conductivity and poor activity. From the perspective of electronic structure modification, oxygen-incorporated Ni aerogel is prepared by a facile reduction-oxidation method. With the optimized electronic structure in Ni@NiO-2 aerogel by oxygen incorporation, brilliant photocatalytic activity with CO yield of 39.30 μmol/mg and CO selectivity of 94.4 % could be achieved, taking advantage of the electron-rich Ni and greatly increased conductivity as well as sufficient active sites exposure. This work sheds light on the design and development of high-performance non-noble metal-based systems for catalytic CO₂ utilization.

1. Introduction

Voluminous dependence on fossil fuels has caused extensive greenhouse gas accumulation in the atmosphere, with the consequence of serious environmental problems [1,2]. To figure out this issue, sustainable production of high value-added industrial raw materials such as CO through efficient photocatalytic CO₂ dissociation is proposed as one of the most emerging pathways for environmental pressure alleviation and energy crisis mitigation, yet with the drawback of sluggish reaction kinetics resulting from C-C coupling and multi-electron transfer route [3,4]. Typically, functional noble-metal catalysts with plentiful catalytic active site exposure have been vastly investigated [5,6]; however, owing to their scarcity and high cost, it is of vital necessity to develop efficient and cost-effective alternatives for future large-scale applications.

In this sense, Ni-based catalysts, one of the non-noble-metal alternatives, with merits of impressive performance and superior selectivity, hold notable expectations for photochemical catalysis [7–9]. In spite of these great advances, it remains a long journey for industrial applications from intricate synthesis and limited performance. It has been

demonstrated that the surface active sites and electronic structure both constitute the principal passport to determining photocatalyst performance [10,11]. Recently, metal aerogels (MAs), possessing specific porous three-dimensional (3D) nanostructures, have been shown much solicitude for since marked in 2009, which are endowed with gigantic specific surface areas for superior 3D electron/mass transfer pathways and numerous catalytic active sites exposure [12–15]. On the other hand, element incorporation is effective on surface electronic modulation, like B-doped Bi [16] and O-incorporated NiCoP/Ni₂P [17]. Thereby, it is highly promising to embellish the electronic structure via element incorporation in aerogel-based materials for CO₂ photoreduction.

Herein, we make an attempt to prepare an amorphous Ni@NiO core-shell aerogel with oxygen incorporation modification. In conjunction with the electronically modified Ni, the intrinsic advantages in metal aerogel outstand the CO₂ reduction activities in terms of CO synthetic harvest of 39.30 μmol/mg and CO selectivity of 94.4 %, during a 3 h irradiation. A series of determinations including XPS, Raman and electrochemical analysis are executed to underline the influence of O

* Corresponding author.

** Corresponding author at: School of Environment and Energy, Guangdong Provincial Key Laboratory of Solid Wastes Pollution Control and Recycling, The Key Laboratory of Pollution Control and Ecosystem Restoration in Industry Clusters (Ministry of Education), South China University of Technology, Guangzhou, Guangdong 510006, China.

E-mail addresses: esliangshujie@scut.edu.cn (S. Liang), dengh2016@scut.edu.cn (H. Deng).

incorporation on Ni. In situ FTIR spectra are to demystify the CO₂-CO reaction pathway, while Mott-Schottky plots are performed for photocatalytic mechanism interpretation. These results hold enlightenment and reference meaning for discovering more high-performance photocatalysts.

2. Experimental section

2.1. Chemical and materials

Chemicals used are composed of Nickel (II) chloride hexahydrate (NiCl₂·6H₂O, Aladdin), sodium borohydride (NaBH₄, Aladdin), [Ru(bpy)₃]Cl₂·6H₂O (abbreviated as Ru, bpy = 2,2-bipyridine, Innochem), triethanolamine (TEOA, Aladdin), acetonitrile (MeCN, Aladdin). The gases including ultra-purity carbon dioxide (99.9999 %) and ultra-purity argon (99.9999 %) are purchased from Foshan Ms Messer Gas Co., Ltd. All reagents and chemicals are used without further purification.

2.2. Synthesis of pre-Ni aerogel

The synthesis of pre-Ni aerogel sample is prepared according to the method reported with a slight modification [18]. First, NiCl₂·6H₂O (0.5 mmol) and freshly prepared NaBH₄ (1.5 mmol) are dissolved in 5 mL and 15 mL pure water, respectively, to form solutions A and B. Then, solution A is slowly added to solution B to obtain mixture solutions, followed by quick-freezing by liquid nitrogen and subsequent thawing in a water bath for several hours. Afterward, the obtained samples are washed twice with pure water to remove the residual impurities and successively solvent-exchanged with tert-butanol. Prior to being combusted in a muffle furnace (200 °C, 5 °C/min), the samples are thoroughly dried by a freeze dryer (24 h). For comparison, the freshly prepared wet Ni gel is also dried using a vacuum drying oven (Model: DZF-6050) at 50 °C for 12 h.

2.3. Fabrication of Ni@NiO aerogel

The above pre-Ni fabricated is applied as the template for subsequent oxygen incorporation modified by calcination in a muffle furnace at 200 °C. With the ramping rate of 5 °C/min, Ni@NiO-1, Ni@NiO-2, and Ni@NiO-3 aerogels are obtained in air atmosphere, corresponding to distinct heating durations of 0.5, 2 and 4 h.

2.4. Construction of c-Ni, c-Ni@NiO and c-NiO

With the same template of pre-Ni aerogel obtained after freeze drying, the c-Ni, is fabricated after calcinating in N₂ at 200 °C for 2 h. For c-Ni@NiO and c-NiO, both of them are constructed by annealing in the air atmosphere for 2 h, except for diverse temperatures of 400 °C and 600 °C respectively. The corresponding parameters are listed in Table S1.

2.5. Materials characterization

Performed on Bruker D8 AVANCE X-ray diffractometer with Cu K α at a current of 40 mA and a voltage of 40 kV, X-ray diffraction (XRD) data are collected to study the component and crystallinity of the as-synthesized aerogels. Carried out by a Thermo Fisher Escalab 250Xi X-ray instrument with Al K α radiation, X-ray photoelectron spectroscopy (XPS) is employed to disclose the element species as well their valence states on the aerogel surfaces. To clearly observe the morphology of the materials, the images from field emission scanning electron microscopy (FE-SEM, Carl Zeiss MERLIN) as well as transmission electron microscopy (TEM, JEM-2100, JEOL Ltd.) are recorded. As for the fine structure and element distribution, high-resolution TEM images (HRTEM) with elemental mapping are further conducted to obtain relative information. ¹H NMR spectrum is recorded on a Bruker AC-400FT

spectrometer at 400 MHz. An Agilent 7890B-5977A gas chromatography-mass spectrometry (GC-MS) system is utilized to conduct ¹³CO₂ isotopic experiment and analyze its corresponding gaseous products with ¹³CO₂ replacement of ¹²CO₂. An Edinburgh FL/FS900 instrument is conducted to record the photoluminescence (PL) spectra under 540 nm laser irradiation. Electrochemical measurements containing electrochemical impedance spectroscopy (EIS) and linear sweep voltammetry (LSV) are carried out in a 0.1 M Na₂SO₄ solution saturated with Ar or CO₂ configured by a typical three-electrode system: the prepared Ni@NiO aerogel-modified FTO glass at the working electrode, Pt as the counter electrode and saturated glycury electrode as the reference electrode. Cyclic voltammetry (CV) is conducted at a scan rate of 100 mV/s in an Ar-saturated 1 M KOH, with Hg/HgO electrode as the reference electrode. The Brunauer-Emmett-Teller (BET) surface area is analyzed by nitrogen adsorption/desorption isotherms with the operation on Micromeritics ASAP 2020 analyzer. And the CO₂ adsorption isotherms are collected on the same analyzer at 298 K in a CO₂ atmosphere. Aiming at analyzing the diversity in the chemical composition of the material, Raman spectroscopy (DXR 2xi, Thermo) is collected. Range from 4 cm⁻¹ to 4000 cm⁻¹, in-situ Fourier Transform Infrared Spectroscopy (in situ FTIR) is real-time recorded on an infrared spectrometer (Nicolet Nexus 670) with CO₂ as the probe under light irradiation. With the conduction on a UV 2600 spectrometer (Shimadzu, Japan), DRS UV-vis diffuse reflectance spectra (DRS) are obtained. Implemented at a constant 15 kHz between potentials of -0.8 V and 0.8 V, Mott-Schottky plots are acquired.

2.6. Photocatalytic CO₂ reduction

The study of the photocatalytic activities of the Ni@NiO aerogels towards CO₂ reduction is carried out in a solid-liquid two-phase system under the condition of ambient temperature and pressure. The catalysts (certain dose) and the photosensitizer [Ru(bpy)₃]Cl₂·6H₂O (7.5 mg) are aggregated in an acetonitrile/water/triethanolamine (3 mL/2 mL/1 mL) solution in a gas-closed quartz reactor (capacity of 75 mL), which is entirely vacuum degassed followed by subsequent backfilled of ultra-pure CO₂ (99.9999 %) before reaction. To supply a light source, a multiple-channel system for parallel reaction (PCX50A Discover), equipped with a 5 W LED lamp (400–1000 nm), is applied during the process, which is purchased from Beijing Perfect Light Company, China. The built-in fans and magnetic stirrers contribute to the constant temperature and complete dispersion during the whole photocatalytic reaction. After illumination, the extracted gas is purged into gas chromatography (Agilent 7890B) for component distinguishment. For the conduction of recycling tests, the recycled samples with repeated washing are introduced into the same system to start the next cycle. Relative calculations including CO selectivity and apparent quantum efficiency (A.Q.E.) under 420 nm with a 3 cm² illuminated area are determined by the following formulas,

$$\text{CO selectivity} = \frac{\text{number of CO generated}}{\text{number of H}_2 \text{ evolved} + \text{number of CO generated}} \times 100\%$$

$$\text{A.Q.E.(\%)} = \frac{2 \times \text{number of CO generated}}{\text{number of incident electrons}} \times 100\%$$

3. Results and discussion

3.1. Materials synthesis and characterizations

The Ni@NiO aerogels are prepared through a sequential reduction-oxidation route with NiCl₂·6H₂O as the metal source and NaBH₄ as a reducing agent (Fig. 1a). By tuning the annealing duration yet keeping the temperature constant at 200 °C in the air atmosphere, a series of samples are fabricated and defined as Ni@NiO-1, Ni@NiO-2, Ni@NiO-3, respectively. Besides, their counterparts including c-Ni (crystalline-Ni),

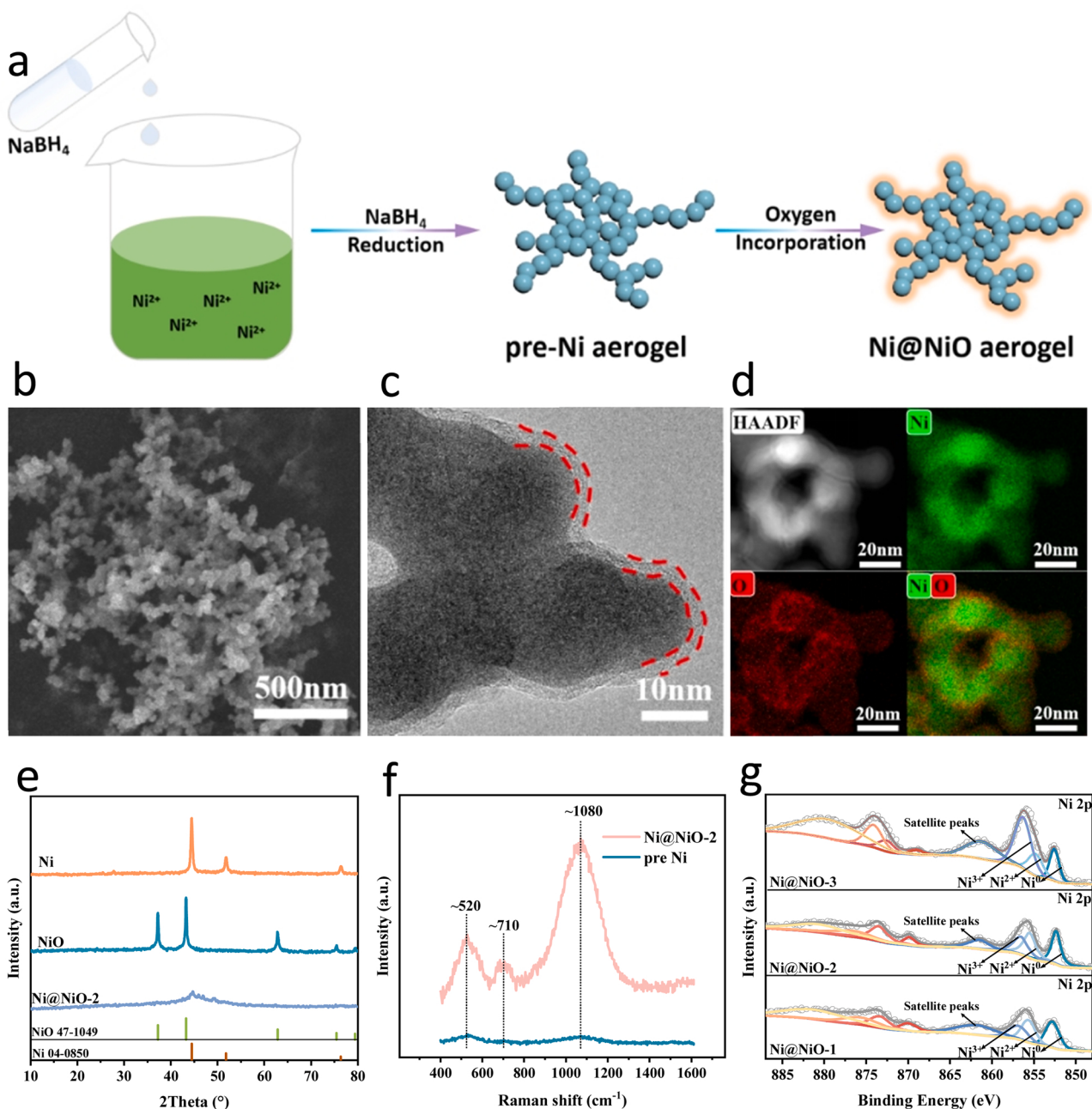


Fig. 1. (a) Schematic illustration of preparation of Ni@NiO aerogels. (b) SEM image, (c) HRTEM image, and (d) STEM-EDS mapping images of the Ni@NiO-2 aerogel. (e) XRD patterns of c-Ni, c-NiO, c-Ni@NiO, and Ni@NiO-2 aerogel, (f) Raman spectra of Ni aerogel before and after oxygen incorporation. (g) Ni 2p XPS spectra of Ni@NiO aerogels. (Red dashed line in c) is to distinguish core-shell structure.

c-NiO (crystalline-NiO) and c-Ni@NiO (crystalline-Ni@NiO) are also obtained for comparison, whose annealing details are listed in Table S1.

The macroscale morphology (Fig. S1) of the resulting Ni@NiO samples present self-supported monolithic aggregated structures, ascribed to the successful preparation of lightweight bulk aerogels [18]. Corresponding investigations by scanning electron microscopy (SEM) in Fig. 1b and Fig. S2 are employed to verify the original structure preservation of hierarchical porous interconnected network by cross-linking nanowires, free from annealing interference. Noteworthy, high-resolution transmission electron microscopy (HRTEM) of Ni@NiO-2 in Fig. 1c highlights the amorphous characteristics of core-shell structures, with the existence of a conspicuous oxidation layer and zero distinguishable lattice fringes. Additionally, high-angle annular dark-field (HAADF)-STEM image and the corresponding

energy-dispersive X-ray spectroscopy (EDS) elemental mapping on Ni@NiO-2 certify the existence and dispersion of Ni and O elements, confirming the successful epitaxial-growth of oxidized shell over metallic Ni core (Fig. 1d).

XRD patterns show that all Ni@NiO samples, independent of the annealing duration, exhibit unique broad diffraction peaks at around 45° similar to pre-Ni ones in Fig. 1e and Fig. S3, again indicating the amorphous character maintenance after controlled calcination. However, it could not be neglected that the peak is gradually left-shifted with increased calculation time, suggesting the enhanced engagement of oxygen element. Contrastingly, as seen from Fig. 1e, c-Ni, c-NiO and c-Ni@NiO all demonstrate well-defined crystalline nature (JCDPS card nos.: 04-0850 and 47-1049), which may expose fewer active defect sites than amorphous ones and thus weaken catalytic activity [19].

Furthermore, as depicted in Fig. 1f, the Raman profile of the synthesized Ni@NiO-2 aerogels in the spectral range of 400–1600 cm⁻¹, with three major peaks in good agreement with the reported values of the NiO phase, could be distinguished and centered at ~ 520 cm⁻¹ (first-order transverse optical mode, i.e. TOM), ~ 710 cm⁻¹ (longitudinal optical mode, i.e. LOM)), and ~ 1080 cm⁻¹ (second-order transverse optical mode, i.e. 2TOM), respectively [20,21]. The differences existing in the samples before and after annealing reveal the incorporation of oxygen into the as-prepared aerogel, further conducive to modulating the electronic environment of Ni element. Moreover, Raman analysis over distinct Ni@NiO aerogels is also executed (Fig. S4), where the peak intensity of Ni@NiO-2 is significantly higher than the other ones. As the peaks observed are ascribed to NiO phase [20], it could be concluded that Ni²⁺ species are preponderantly distributed on Ni@NiO-2 surface rather than Ni@NiO-1 and Ni@NiO-3. In the meanwhile, it also indicates that the local environment of Ni is successfully embellished by Ni-O interaction modification.

To better disclose the Ni-O interaction, XPS data are collected. As shown in Fig. S5, the as-obtained Ni@NiO aerogels consisted of Ni and O elements with near-identical full-spectrum (C element originating from ineluctable atmospheric carbon contamination). The high-resolution Ni 2p signal spectrum is further studied to determine the electronic states in Fig. 1g, with 2p_{3/2} main peak deconvoluted into three peaks at 852.5, 855.6 and 856.6 eV, stemming from Ni⁰, Ni²⁺, and Ni³⁺ [22,23]. Clearly, the prevailing Ni species undergo a revolution (Ni⁰→Ni²⁺→Ni³⁺) with annealing-time extension from 0.5 h to 4 h (seen from Table S2), indicating that the electronic structure modification of Ni is achieved by tunable oxygen-incorporated process [24]. Moreover, XPS analysis is also conducted over NiO and Ni in Fig. S6, both of whom demonstrate distinctive feature from Ni@NiO ones [25]. Generally, Ni of high valence state, would weaken the binding energy of CO on the catalyst surface and hence strengthen resistance to CO poisoning, compared to metallic Ni, for activity consolidation [26].

These results above prove the formation of amorphous Ni@NiO core-shell aerogels and the modification of Ni electronic structure.

We further conduct cyclic voltammetry (CV) measurements of aerogels in Ar-saturated 1 M KOH solution at 100 mV/s (Fig. S7). Notably, a pair of distinct redox peaks in a potential window ranging from 0.3 to 0.5 V vs. Hg/HgO could be easily distinguished, corresponding to Ni²⁺/Ni³⁺ redox couple [27,28]. Among the catalyst tested, Ni@NiO-2 shows off the highest anodic and cathodic peak intensity, manifesting the adequate and accessible exposure of active sites [29]. Following the scan direction, a wave at 0.45 V vs. Hg/HgO, assigned to the Ni²⁺→Ni³⁺ oxidation, emerges firstly during the anodic sweep, while a wave for Ni³⁺→Ni²⁺ is found at 0.32 V vs. Hg/HgO for reversal cathodic scan. The considerably high oxidation peak for Ni@NiO-2 implies the abundant coverage of Ni²⁺ species before electrical oxidation.

3.2. Catalytic performance for CO₂ photoreduction

The as-prepared samples perform the CO₂ photoreduction reaction over 3 h with [Ru(bpy)₃]Cl₂·6H₂O in MeCN/H₂O/TEOA mixed solution in Fig. 2. The election of the solution system is grounded on the medium property, where MeCN acts as favorable CO₂ dissolving agent, yet H₂O is devoted to being the reaction kinetics promoter [30,31]. To quantify the optimum catalyst dosage, the effect of Ni@NiO-2 input on the yield of photocatalytic reduction products is determined (Fig. S8). Both CO and H₂ emerge as primary gaseous stock during the catalytic progress; as for the liquid products determination, ¹H NMR spectrum in Fig. S9, confirms that no liquid hydrocarbon production is carried on, consistent with the results found by the previously reported works [32]. When performed with the lack of any catalysts, the system brings about scarce products of 1.49 μmol/mg CO with 68.2 % selectivity. With the augmenting addition of Ni@NiO-2 from 0 mg to 1.5 mg, the trend for CO yield shows a vivid volcano shape. Remarkably, with 0.7 mg catalyst engaged, the catalytic system exhibits the highest CO yield of

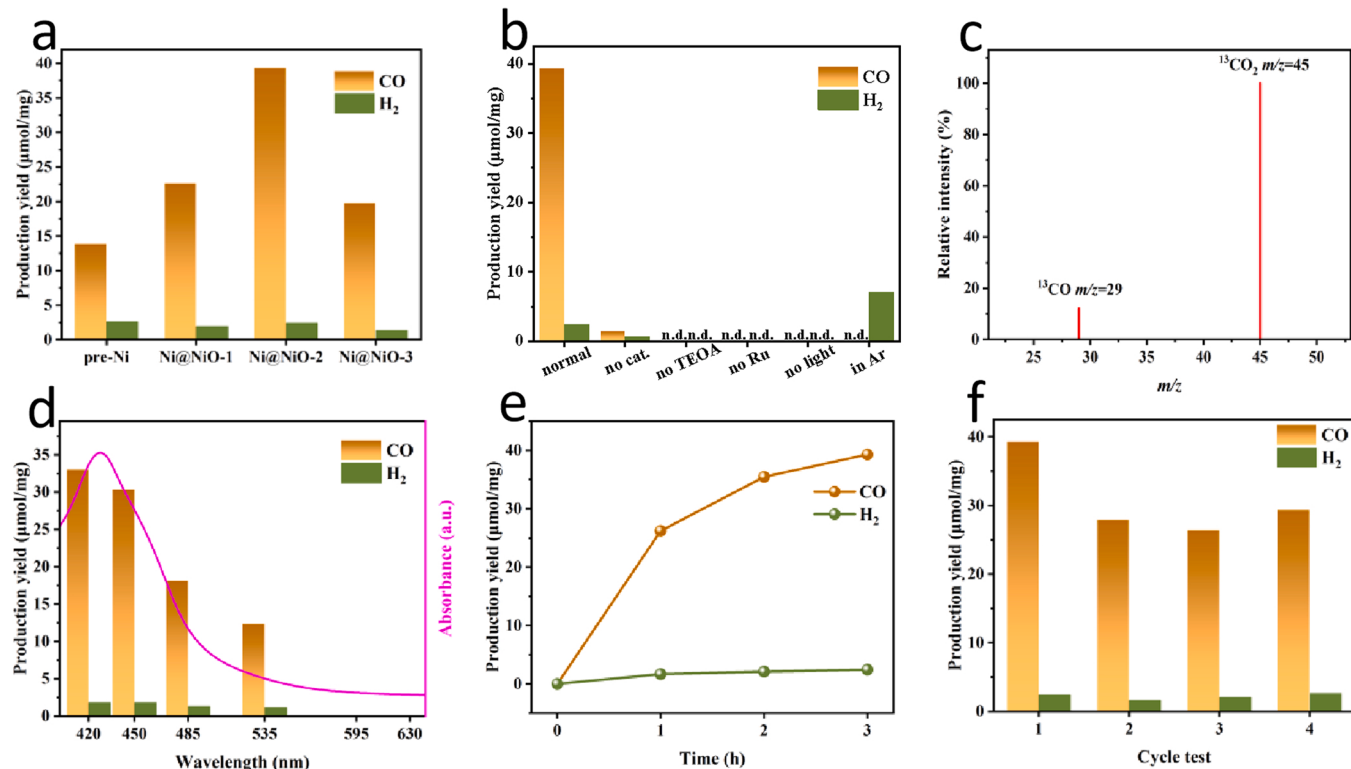


Fig. 2. (a) Evolution of CO and H₂ for pre-Ni and Ni@NiO aerogels during 3 h photoreduction. (b) Evolution of CO and H₂ of the Ni@NiO-2 under various reaction conditions. (c) The isotope analysis of CO using ¹³CO₂ as carbon source by GC-MS. (d) Wavelength-dependent of the CO and H₂ generation for Ni@NiO-2. (e) Production of CO and H₂ as a function of reaction time over Ni@NiO-2. (f) Stability tests for Ni@NiO-2.

39.30 $\mu\text{mol}/\text{mg}$ and CO selectivity of 94.4 %, reaching 26 and 1.4 times that of the blank control. To our knowledge, the value is much higher than most previously reported non-noble metal based photocatalysts for CO_2 reduction (Table S3). After that, the yield of products declines with the further increase of aerogel dosage; such progression of firstly increased and then decreased is principally in view of the shading effect from superfluous catalyst dosage [33]. As the consequence, the optimal dosage is laid down at 0.7 mg for subsequent photocatalytic studies.

The CO_2 photoreduction activities of pre-Ni and Ni@NiO aerogels are tested in Fig. 2a, where all Ni@NiO samples with oxygen incorporation accumulate more CO output under the identical irradiation conditions than pre-Ni, verifying the vital influence of oxygen incorporation on the photocatalytic performance toward CO_2 reduction. Specifically, it could be witnessed that Ni@NiO-2 has excellent catalytic activity with a maximum CO yield of 39.30 $\mu\text{mol}/\text{mg}$, indicating more efficient CO_2 catalysis on Ni@NiO-2 compared to that on Ni@NiO-1 and Ni@NiO-3. Among the Ni@NiO samples, the lowest CO harvest of 18.13 $\mu\text{mol}/\text{mg}$ is illustrated over Ni@NiO-1, with Ni^0 acting as the popular species (seen from XPS), whose reason may lie in the deficiency of annealing duration, hence bringing about insufficient oxygen-incorporation. This consequence is consistent well with early reports, as CO desorption acting as a Rate Determining Step during the whole CO_2 -reduction process, would be hampered by metallic nickel compared to oxidized Ni [26,34]. On the other hand, when the oxygen-incorporation extent is excessively strengthened by annealing the pre-Ni in the air for 4 h, the prevailing formation of Ni^{3+} species, might impede the interaction between Ni^{2+} and CO_2 and thus possibly proclaim the efficiency decline in Ni@NiO-3. The above results imply that appropriate oxygen-incorporation extent is of significance for CO_2 -CO conversion activity, and Ni^{2+} might be deemed to be the intrinsic active specie with satisfactory competitiveness. Therefore, it can be concluded that the dramatically improved photocatalytic property is obtained through facile oxidized state modulation on surficial Ni species [35]. As for the crystal samples (Fig. S10), the CO outputs reach 10.28 $\mu\text{mol}/\text{mg}$ for c-Ni, 12.85 $\mu\text{mol}/\text{mg}$ for c-NiO and 18.13 $\mu\text{mol}/\text{mg}$ for c-Ni@NiO respectively, all of which are considerably lower than the amorphous Ni@NiO-2. This result highlights the advantage of abundant defect sites of the amorphous material as well as the core-shell heterostructures.

Furthermore, a range of contrast experiments is designed to comprehensively figure out the relationship between catalytic conditions and performance, and the outcomes are displayed as followed in Fig. 2b. When conducting the normal test with Ni@NiO-2 as the photocatalyst (column 1), the CO generation yield is up to 39.30 $\mu\text{mol}/\text{mg}$, which significantly exceed the outcome of the system without any catalyst (column 2). This result reveals the crucial role that catalysts played in the catalytic process. With the system created in a TEOA/Ru/light-free condition (columns 3–5), the negligible gas product is detected, suggesting the indispensable role of an electronic sacrificial agent (TEOA), and that the whole process is driven and operated by light-irradiation over Ru photosensitizer. Once the CO_2 is replaced with ultrapure Ar (column 6), only a few H_2 could be caught, which confirms the unique source of CO among the products; such a phenomenon is in line with the results of other literature [36]. In addition, for forthrightly tracing the CO source, the isotopic-label experiment is carried to completion and exhibited in Fig. 2c and Fig. S11. With $^{13}\text{CO}_2$ as the initial carbon source, the signal for ^{13}CO at $m/z = 29$ could be evidently discerned, testifying that the definite origin of CO from CO_2 transformation [37,38].

Additionally, to disclose the wavelength-relevant impact, performance evaluations are performed under five variant single-wavelength light sources in Fig. 2d. Distinctly, the trend for CO production yield basically coincides with the trend of the absorption spectrum of the Ru photosensitizer, further confirming that the photocatalytic CO_2 reaction is indeed initiated by visible light excitation of the photosensitizer. Determined with an optical power meter, the apparent quantum efficiency (A.Q.E.) relative to CO of the reaction system is calculated up to

1.50 % (under 420 nm).

To understand the stability and reusability of the catalysts, which are two indispensable representatives for evaluating the catalyst performance, we firstly conduct an exploration of the photocatalytic synthetic yield vs. extended time. As displayed in Fig. 2e, the production rates of CO and H_2 reach their peaks during the first hour of the reaction. Afterward, the generation rates become lower and lower, the reason for which may lie in the continuous consumption of photosensitizers [39, 40]. To demonstrate this phenomenon, the reactivation experiment is conducted with the same-dose supplement of photosensitizer. As evidenced by Fig. S12, its photocatalytic activity approximates to that of the initial reaction, indeed confirming that a diminution in CO productivity at the latter stage of the reaction is ascribed to photosensitizer deactivation. Ni@NiO-2 further is recovered after a 3 h photocatalytic test, and exploited repeatedly in the recycling CO_2 reduction reactions. Despite a modest activity drop detected for the second test, steady preservation in the photocatalytic performance is observed for several subsequent recycling tests (see Fig. 2f). With auxiliary analysis of XRD and FESEM characterizations displayed in Fig. S13, it could be supposed that a fragile framework collapse takes place after the first test, possibly resulting in a performance decline. However, the as-formed structure remains stable in the following cycles with essentially similar CO yield produced, and simultaneously, few noticeable alternation between the fresh and used samples is detected in XRD patterns. The above analysis validates the eligible stability and feasible repeatability of the Ni@NiO-2 sample in the photocatalytic system.

Moreover, the bulky counterpart prepared with a vacuum hot dryer is also fabricated and tested to validate the influence of specific 3D nanowire network. The porous channel network is substituted by nanosheet-assembled bulk (Fig. S14), and the latter exhibits conspicuous CO-turnout recession compared to that produced in the freeze dryer, which could be attributed to weakened active site accessibility from structure collapse. Similar results have been identified in previous work [41].

3.3. Enhanced mechanism exploration

As demonstrated in Nyquist plots of pre-Ni and Ni@NiO-2 (Fig. 3a), a smaller diameter of the semicircle for Ni@NiO-2 implies a lower electron-transfer resistance than that of pre-Ni, revealing the upgraded conductivity of Ni@NiO-2 aerogel due to the oxygen incorporation [42]. The conductivity promotion discloses the electronic structure alteration of Ni@NiO after O-incorporation [43]. To deeply understand the real electronic structure of Ni@NiO-2 during CO_2 photoreduction, in situ FTIR spectroscopy study is carried out (Fig. 3b & 3c). Compared with pre-Ni, the characteristic band is blueshifted at Ni@NiO-2, which gives straight evidence of the formation of electron-rich Ni originating from oxygen incorporation. The reaction pathway of CO_2 -CO photoconversion has hitherto remained ambiguous, as its process involves multiple electrons and protons transfer. Yet with the real-time detection of intermediates by in situ FTIR during the reaction, it may be likely to uncover the mask from mystery.

As demonstrated in Fig. 3c, the detections of monodentate carbonate groups (m-CO_3^2-) at 1417, 1461, 1496 and 1502 cm^{-1} , bidentate carbonate (b-CO_3^2-) at 1338 and 1361 cm^{-1} , as well as bicarbonate (HCO_3^2-) at 1396, 1423, and 1434 cm^{-1} , all stemming from CO_2 adsorption, highlight the good CO_2 uptake ability [44,45]. A new peak at 1540 cm^{-1} , assigned to the COOH^* groups, is remarkably observed, whose peak intensity visibly increased with the accumulation of irradiation time, hence implying the role of COOH^* groups plays as intermediates, in the process during CO_2 -CO photoreduction [46,47]. Moreover, the peaks at 2065 and 2137 cm^{-1} with intensity increase over time, could be contributed to CO^* and CO absorption respectively, further evidencing the formation of CO product [44,46]. Based on these analyzes, the CO photosynthesis from CO_2 upon Ni@NiO-2 aerogel could be inferred to undergo through the pathways displayed below: 1)

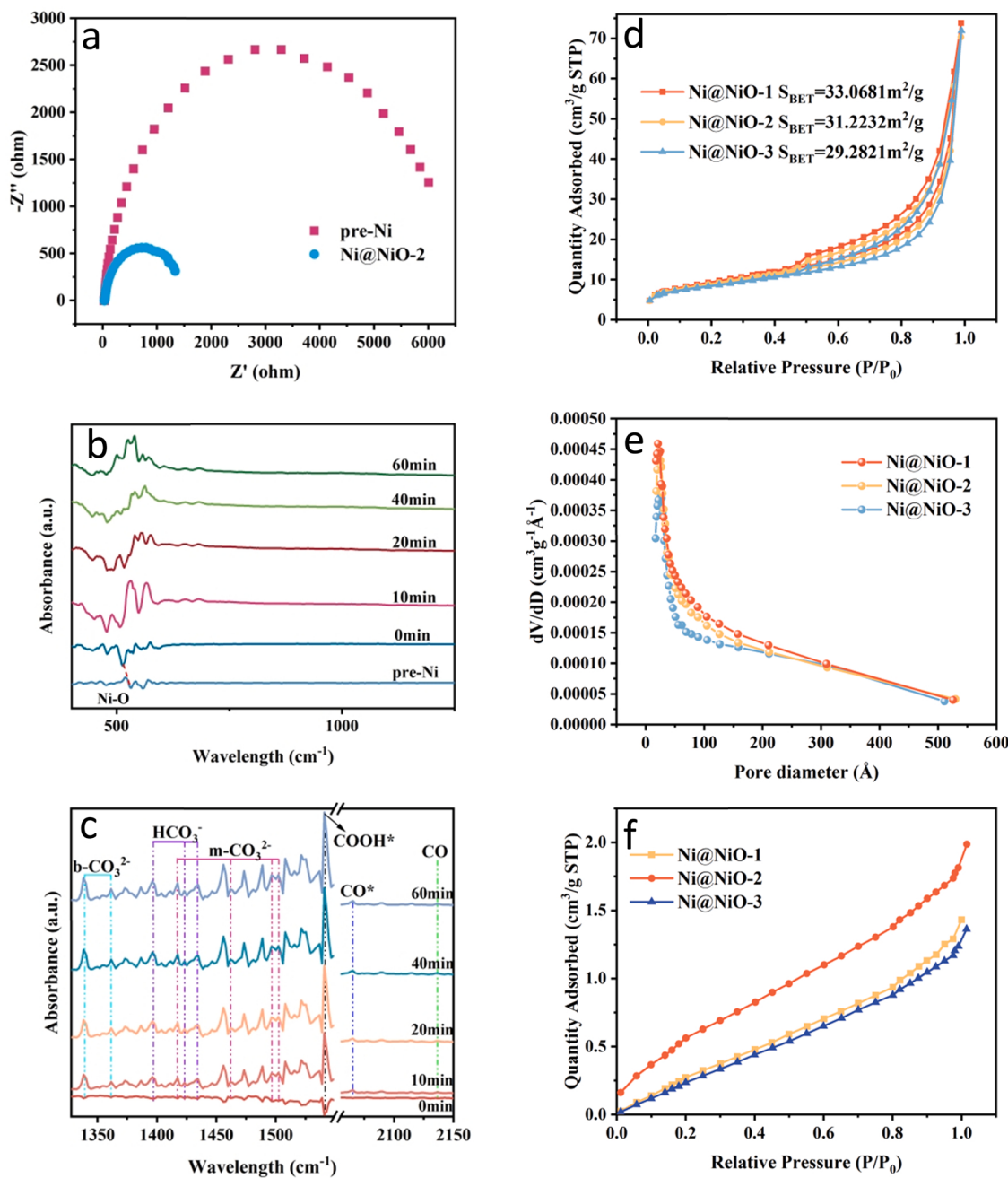


Fig. 3. (a) Nyquist plots of pre-Ni and Ni@NiO-2. (b, c) In situ FTIR spectra on Ni@NiO-2. (d) N₂ adsorption-desorption isotherms and corresponding BET values of Ni@NiO aerogels. (e) Pore size distribution plots. (f) CO₂ adsorption isotherms.

CO₂ adsorption and activation upon the aerogel surface (*+ CO₂→CO₂*, * stands for Ni@NiO-2 aerogel catalyst); 2) interaction between CO₂* and surface proton (originated from H₂O dissociation) for gradual formation of COOH* intermediate (CO₂*+ H⁺ + e⁻→COOH*); 3) COOH* deprotonation into CO* and final CO generation(COOH*+ H⁺ + e⁻→CO* + H₂O, CO*→*+ CO).

In our cases, the specific surface area and porosity are also tested (Fig. 3d & 3e), though the results observed do not make a big difference among the as-synthesized samples. As for the CO₂ adsorption measurements displayed in Fig. 3f, Ni@NiO-2 does express a good CO₂ adsorption performance of 1.99 cm³/g under 1 atm, surpassing Ni@NiO-1 (1.43 cm³/g) and Ni@NiO-3 (1.36 cm³/g). This outcome coincides with the above in situ FTIR analysis, and it could be possibly believed that the electronic structure of Ni would induce somewhat disparity in Ni-CO₂ interaction, which is assumed as the prerequisite for CO₂

photocatalytic reaction [48,49], again foregrounding the germane relationship between the electronic structure of Ni and catalytic performance.

Considering the explicit correlation between photogenerated carrier separation-reconfiguration and photocatalytic activity [50,51], photochemical measurements including steady-state photoluminescence (PL) and linear sweep voltammetry (LSV) are implemented to study the behaviors of photo-generated charge in the system (displayed in Fig. 4a & 4b). Compared to a recognizable characteristic emission peak of photosensitizer Ru observed for the blank system [33], all curves for Ni@NiO show obvious fluorescence quenching at this position, among which Ni@NiO-2 is endowed with the lowest PL intensity. It could be supposed that a robust charge separation ability improvement is obtained by catalyst involvement, and strikingly the most powerful charge separation and electron transfer between the Ru complex and Ni species

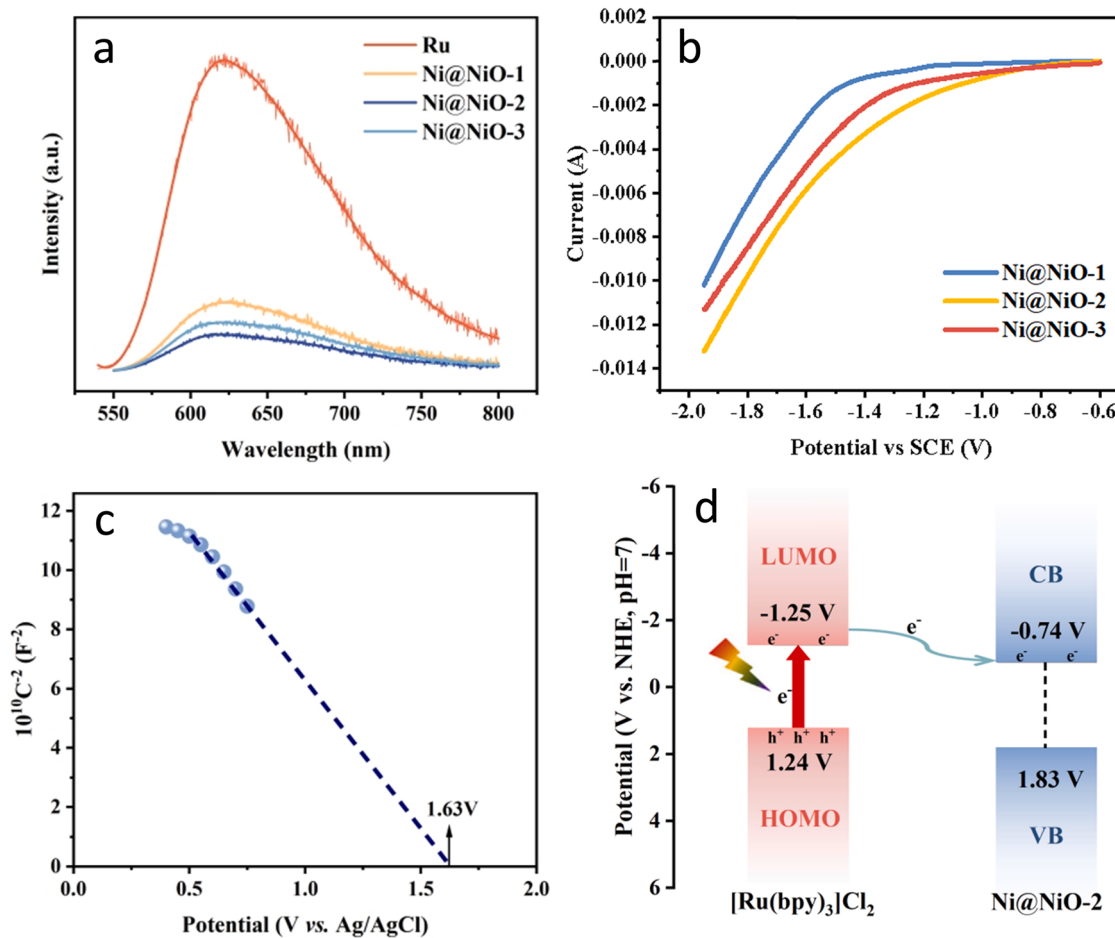


Fig. 4. (a) PL spectra in the blank system, Ni@NiO-1, Ni@NiO-2, and Ni@NiO-3, respectively. (b) LSV plots of Ni@NiO samples in CO₂-saturated KHCO₃ solution. (c) Mott-Schottky plots of Ni@NiO-2. (d) Energy-level alignment of the Ni@NiO-2 aerogel and [Ru(bpy)₃]Cl₂ for CO₂ photoreduction.

is ascribed to Ni@NiO-2 [52,53]. In addition, LSV analysis reveals a considerably lower current density for the Ni@NiO-2 aerogel compared to the contrast samples throughout the potential range (Fig. 4b) [54]. The results above consequently point out that relatively preponderate Ni²⁺ over Ni@NiO-2 by appropriate oxygen-incorporation tuning, is conducive to high-efficient charge transport and separation for excellent CO₂-CO photoreduction.

To interrogate the photocatalytic mechanism, further behavior investigations of the photoinduced charges in Ni@NiO-2 sample by UV-vis diffuse reflectance spectra (DRS) and Mott-Schottky plot are acquired. The optical absorption properties of the Ni@NiO-2 samples are shown in Fig. S15, being characteristic of black solid [55], and consequently, the corresponding band gap (E_g) value calculated from Kubelka-Munk function is obtained to be 2.57 eV. The flat band potential is derived firstly by Mott-Schottky plots in Fig. 4c, whose negative slope manifests the p-type semiconductor feature of the material. According to the Mott-Schottky formula, the flat band potential (E_{fb}) is identified at 1.63 V (vs. Ag/AgCl), also proclaiming 1.63 V (vs. Ag/AgCl) or 1.83 V (vs. NHE, pH = 7) for valence band (VB), for that E_{fb} closely approximates to E_{VB} for p-type semiconductors [56,57]. Attributed to the equation of E_{CB} = E_{VB} - E_g, the conduction band edge is accordingly deemed to be -0.74 V (vs. NHE, pH = 7) for E(Ru^{*/Ru}) and -0.53 V (vs. NHE, pH = 7) for E(CO₂/CO). As a consequence, the photoexcited electrons generated under illumination have a thermodynamical advantage over transferring from photosensitizer to Ni@NiO-2 and subsequently to the CO₂ adsorbed, whose scheme of energy levels and electron transfer pathways is illustrated in Fig. 4d.

Keeping the abovementioned discussions in mind, we propose a

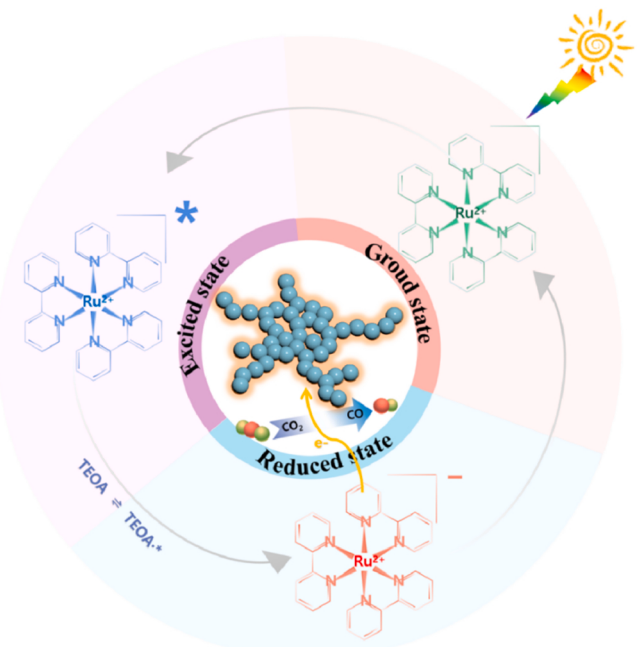


Fig. 5. Proposed mechanism of photocatalytic reduction of CO₂ by Ni@NiO-2 aerogel photocatalyst under light irradiation.

reaction scheme as shown in Fig. 5, explaining the mechanism of photocatalytic cycles on Ni@NiO-2 aerogel material. Under visible-light illumination, the excitation of photosensitizer Ru is initiated, giving rise to Ru^{*}. As an elevated active proton donor, Ru^{*} could be then quenched by the readily available TEOA (a sacrificial electron donor), followed by the conversion into reduced Ru⁺. On account of the pertinent energy gap between Ru sensitizer and co-catalyst Ni@NiO-2, the photogenerated electron is transferred from Ru to the conduction band (CB) of Ni@NiO-2 [58–60], which would then easily dispersed within the aerogel framework for rapid reductive conversion because of high conductance [61].

4. Conclusions

To be summarized, the amorphous Ni@NiO core-shell aerogel has been rationally constructed and successfully demonstrated as an efficient photocatalyst for CO₂-CO reduction. Ni@NiO-2, with prevailing Ni²⁺ as the potential active site, manifests a gratifying CO yield of 39.30 μmol/mg with CO selectivity up to 94.4 % over 3 h visible light illumination. It is believed that the 3D nanowire-network morphology stemming from the inherent characteristic of aerogel, sufficient active site exposure out of amorphous heterostructure, and favorable electron-structure of Ni created by oxygen-incorporation, synergically effectuate the satisfactory catalytic performance. The reaction pathway is elucidated by in situ FTIR spectroscopy, and moreover, the photocatalytic mechanism is suggested with the assistance of DRS and Mott-Schottky plots. This work revealed the feasibility of electronic modification engineering and shed new light on the design and development of aerogel-based materials for CO₂ utilization.

CRediT authorship contribution statement

Zuqi Zhong: Investigation, Validation, Formal analysis, Writing – original draft, Writing – review & editing. **Haofan Wang:** Visualization, Software. **Shujie Liang:** Conceptualization, Writing – review & editing, Funding acquisition. **Xiaohui Zhong:** Data curation, Conceptualization. **Hong Deng:** Funding acquisition, Conceptualization, Resources, Project administration, Writing – review & editing, Supervision.

Declaration of Competing Interest

The authors declare that they have no known competing financial interests or personal relationships that could have appeared to influence the work reported in this paper.

Data Availability

The authors do not have permission to share data.

Acknowledgments

This work was supported by the China Postdoctoral Science Foundation (No. 2021M701246), and the National Key Research and Development Program of China (Nos. 2019YFC1805902, 2019YFA0210402).

Appendix A. Supporting information

Supplementary data associated with this article can be found in the online version at [doi:10.1016/j.apcatb.2023.122603](https://doi.org/10.1016/j.apcatb.2023.122603).

References

- [1] M. Kou, W. Liu, Y. Wang, J. Huang, Y. Chen, Y. Zhou, Y. Chen, M. Ma, K. Lei, H. Xie, P.K. Wong, Ye Liqun, Photocatalytic CO₂ conversion over single-atom MoN₂ sites of covalent organic framework, *Appl. Catal. B: Environ.* 291 (2021), 120146.
- [2] Y. He, H. Rao, K. Song, J. Li, Y. Yu, Y. Lou, C. Li, Y. Han, Z. Shi, S. Feng, 3D hierarchical ZnIn₂S₄ nanosheets with rich Zn vacancies boosting photocatalytic CO₂ reduction, *Adv. Funct. Mater.* 29 (2019), 1905153.
- [3] H. Zhang, Y. Wang, S. Zuo, W. Zhou, J. Zhang, X.W.D. Lou, Isolated cobalt centers on W₁₈O₄₉ nanowires perform as a reaction switch for efficient CO₂ photoreduction, *J. Am. Chem. Soc.* 143 (2021) 2173–2177.
- [4] Y. Wang, S. Wang, S.L. Zhang, X.W. Lou, Formation of hierarchical FeCoS₂-CoS₂ double-shelled nanotubes with enhanced performance for photocatalytic reduction of CO₂, *Angew. Chem. Int. Ed.* 59 (2020) 11918–11922.
- [5] Y. Ma, X. Yi, S. Wang, T. Li, B. Tan, C. Chen, T. Majima, E.R. Waclawik, H. Zhu, J. Wang, Selective photocatalytic CO₂ reduction in aerobic environment by microporous Pd-porphyrin-based polymers coated hollow TiO₂, *Nat. Commun.* 13 (2022) 1400.
- [6] H. Huang, R. Shi, Z. Li, J. Zhao, C. Su, T. Zhang, Triphase photocatalytic CO₂ reduction over silver-decorated titanium oxide at a gas-water boundary, *Angew. Chem. Int. Ed.* 134 (2022), e202200802.
- [7] X. Xiong, C. Mao, Z. Yang, Q. Zhang, G.I.N. Waterhouse, L. Gu, T. Zhang, Photocatalytic CO₂ reduction to CO over Ni single atoms supported on defect-rich zirconia, *Adv. Energy Mater.* 10 (2020), 2002928.
- [8] K. Song, S. Liang, X. Zhong, M. Wang, X. Mo, X. Lei, Z. Lin, Tailoring the crystal forms of the Ni-MOF catalysts for enhanced photocatalytic CO₂-to-CO performance, *Appl. Catal. B: Environ.* 309 (2022), 121232.
- [9] S. Liang, B. Han, X. Ou, X. Ye, W. Chen, H. Deng, C. Tian, Z. Lin, Lattice-strained nickel hydroxide nanosheets for the boosted diluted CO₂ photoreduction, *Environ. Sci.: Nano* 8 (2021) 2360–2371.
- [10] Q. Wang, L. Dong, M. Li, H. Lu, G. Wei, Y. Qu, G. Wang, Z-scheme heterojunction photocatalyst based on lanthanum single-atom anchored on black phosphorus for regulating surface active sites, therefore enhancing photocatalytic CO₂ reduction with ≈ 100 % CO selectivity, *Adv. Funct. Mater.* 32 (2022), 2207330.
- [11] L. Wang, Y. Zhang, L. Chen, H. Xu, Y. Xiong, 2D polymers as emerging materials for photocatalytic overall water splitting, *Adv. Mater.* 30 (2018), 1801955.
- [12] X. Jiang, R. Du, R. Hübner, H. Yue, A. Eychmüller, A roadmap for 3D metal aerogels: materials design and application attempts, *Matter* 4 (2021) 54–94.
- [13] W. Gao, M. Lei, L. Li, D. Wen, Promoting the electrocatalytic properties of nickel aerogel by gold decoration for efficient electrocatalytic oxygen evolution in alkali, *Chem. Commun.* 56 (2020) 15446–15449.
- [14] C. Kim, K.M. Cho, K. Park, J.Y. Kim, G.-T. Yun, F.M. Toma, I. Gereige, H.-T. Jung, Cu/Cu₂O interconnected porous aerogel catalyst for highly productive electrosynthesis of ethanol from CO₂, *Adv. Funct. Mater.* 31 (2021), 2102142.
- [15] Z. Wu, H. Wu, W. Cai, Z. Wen, B. Jia, L. Wang, W. Jin, T. Ma, Engineering bismuth-tin interface in bimetallic aerogel with a 3D porous structure for highly selective electrocatalytic CO₂ reduction to HCOOH, *Angew. Chem. Int. Ed.* 133 (2021) 12662–12667.
- [16] X. Chen, H. Chen, W. Zhou, Q. Zhang, Z. Yang, Z. Li, F. Yang, D. Wang, J. Ye, L. Liu, Boron dopant induced electron-rich bismuth for electrochemical CO₂ reduction with high solar energy conversion efficiency, *Small* 17 (2021), 2101128.
- [17] Y. Wen, J. Qi, D. Zhao, J. Liu, P. Wei, X. Kang, X. Li, O doping hierarchical NiCoP/Ni₂P hybrid with modulated electron density for efficient alkaline hydrogen evolution reaction, *Appl. Catal. B: Environ.* 293 (2021), 120196.
- [18] R. Du, J.-O. Joswig, R. Hübner, L. Zhou, W. Wei, Y. Hu, A. Eychmüller, Freeze-thaw-promoted fabrication of clean and hierarchically structured noble-metal aerogels for electrocatalysis and photoelectrocatalysis, *Angew. Chem. Int. Ed.* 132 (2020) 8370–8377.
- [19] S. Anantharaj, S. Noda, Amorphous catalysts and electrochemical water splitting: an untold story of harmony, *Small* 16 (2020), 1905779.
- [20] J. Hu, S. Li, Y. Li, J. Wang, Y. Du, Z. Li, X. Han, J. Sun, P. Xu, A crystalline–amorphous Ni–Ni(OH)₂ core–shell catalyst for the alkaline hydrogen evolution reaction, *J. Mater. Chem. A* 8 (2020) 23323–23329.
- [21] F.T. Thema, E. Manikandan, A. Gurib-Fakim, M. Maaza, Single phase Bunseite NiO nanoparticles green synthesis by Agathosma betulina natural extract, *J. Alloy. Compd.* 657 (2016) 655–661.
- [22] H. Li, Y. Han, H. Zhao, W. Qi, D. Zhang, Y. Yu, W. Cai, S. Li, J. Lai, B. Huang, L. Wang, Fast site-to-site electron transfer of high-entropy alloy nanocatalyst driving redox electrocatalysis, *Nat. Commun.* 11 (2020) 5437.
- [23] R.-T. Gao, D. He, L. Wu, K. Hu, X. Liu, Y. Su, L. Wang, Towards long-term photostability of nickel hydroxide/BiVO₄ photoanodes for oxygen evolution catalysts via in situ catalyst tuning, *Angew. Chem. Int. Ed.* 132 (2020) 6272–6277.
- [24] X. Long, C. Feng, S. Yang, D. Ding, J. Feng, M. Liu, Y. Chen, J. Tan, X. Peng, J. Shi, R. Chen, Oxygen doped graphitic carbon nitride with regulatable local electron density and band structure for improved photocatalytic degradation of bisphenol A, *Chem. Eng. J.* 435 (2022), 134835.
- [25] Z. Yu, K. Yang, C. Yu, K. Lu, W. Huang, L. Xu, L. Zou, S. Wang, Z. Chen, J. Hu, Y. Hou, Y. Zhu, Steering unit cell dipole and internal electric field by highly dispersed Er atoms embedded into NiO for efficient CO₂ photoreduction, *Adv. Funct. Mater.* 32 (2022), 2111999.
- [26] B. Zhao, B. Yan, Z. Jiang, S. Yao, Z. Liu, Q. Wu, R. Ran, S.D. Senanayake, D. Weng, J.G. Chen, High selectivity of CO₂ hydrogenation to CO by controlling the valence state of nickel using perovskite, *Chem. Commun.* 54 (2018) 7354–7357.
- [27] J. Li, Y. Zuo, J. Liu, X. Wang, X. Yu, R. Du, T. Zhang, M.F. Infante-Carrió, P. Tang, J. Arbiol, J. Llorca, Z. Luo, A. Cabot, Superior methanol electrooxidation performance of (110)-faceted nickel polyhedral nanocrystals, *J. Mater. Chem. A* 7 (2019) 22036–22043.
- [28] H. Li, X. Chen, E. Zalnezhad, K.N. Hui, K.S. Hui, M.J. Ko, 3D hierarchical transition-metal sulfides deposited on MXene as binder-free electrode for high-performance supercapacitors, *J. Ind. Eng. Chem.* 82 (2020) 309–316.

[29] A.A. Dubale, Y. Zheng, H. Wang, R. Hübner, Y. Li, J. Yang, J. Zhang, N.K. Sethi, L. He, Z. Zheng, W. Liu, High-performance bismuth-doped nickel aerogel electrocatalyst for the methanol oxidation reaction, *Angew. Chem. Int. Ed.* 59 (2020) 13891–13899.

[30] S. Wang, B.Y. Guan, X.W.D. Lou, Construction of ZnIn₂S₄–In₂O₃ hierarchical tubular heterostructures for efficient CO₂ photoreduction, *J. Am. Chem., Soc.* 140 (2018) 5037–5040.

[31] S. Liang, X. Zhong, Z. Zhong, B. Han, W. Chen, K. Song, H. Deng, Z. Lin, Biomimetic inspired porphyrin-based nanoframes for highly efficient photocatalytic CO₂ reduction, *Chem. Eng. J.* 411 (2021), 128414.

[32] B. Han, X. Ou, Z. Zhong, S. Liang, H. Deng, Z. Lin, Rational design of FeNi bimetal modified covalent organic frameworks for photoconversion of anthropogenic CO₂ into widely tunable syngas, *Small* 16 (2020), 2002985.

[33] W. Chen, B. Han, C. Tian, X. Liu, S. Liang, H. Deng, Z. Lin, MOFs-derived ultrathin holey Co₃O₄ nanosheets for enhanced visible light CO₂ reduction, *Appl. Catal. B: Environ.* 244 (2019) 996–1003.

[34] W. Zhu, S. Kattel, F. Jiao, J.G. Chen, Shape-controlled CO₂ electrochemical reduction on nanosized Pd hydride cubes and octahedra, *Adv. Energy Mater.* 9 (2019), 1802840.

[35] Z.-Y. Wu, W.-B. Ji, B.-C. Hu, H.-W. Liang, X.-X. Xu, Z.-L. Yu, B.-Y. Li, S.-H. Yu, Partially oxidized Ni nanoparticles supported on Ni-N co-doped carbon nanofibers as bifunctional electrocatalysts for overall water splitting, *Nano Energy* 51 (2018) 286–293.

[36] X. Lin, S. Wang, W. Tu, Z. Hu, Z. Ding, Y. Hou, R. Xu, W. Dai, MOF-derived hierarchical hollow spheres composed of carbon-confined Ni nanoparticles for efficient CO₂ methanation, *Catal. Sci. Technol.* 9 (2019) 731–738.

[37] Y. Wang, S. Wang, X.W. Lou, Dispersed nickel cobalt oxyphosphide nanoparticles confined in multichannel hollow carbon fibers for photocatalytic CO₂ reduction, *Angew. Chem. Int. Ed.* 58 (2019) 17236–17240.

[38] G. Chen, F. Wei, Z. Zhou, B. Su, C. Yang, X.F. Lu, S. Wang, X. Wang, Phase junction crystalline carbon nitride nanosheets modified with CdS nanoparticles for photocatalytic CO₂ reduction, *Sustain. Energy Fuels* 7 (2023) 381–388.

[39] S. Wang, B.Y. Guan, X.W.D. Lou, Rationally designed hierarchical N-doped carbon@NiCo₂O₄ double-shelled nanoboxes for enhanced visible light CO₂ reduction, *Energy Environ. Sci.* 11 (2018) 306–310.

[40] J. Qin, L. Lin, X. Wang, A perovskite oxide LaCo₃O₇ cocatalyst for efficient photocatalytic reduction of CO₂ with visible light, *Chem. Commun.* 54 (2018) 2272–2275.

[41] L. Lu, X. Sun, J. Ma, D. Yang, H. Wu, B. Zhang, J. Zhang, B. Han, Highly efficient electroreduction of CO₂ to methanol on palladium-copper bimetallic aerogels, *Angew. Chem. Int. Ed.* 130 (2018) 14345–14349.

[42] C. Yang, Q. Li, Y. Xia, K. Lv, M. Li, Enhanced visible-light photocatalytic CO₂ reduction performance of ZnIn₂S₄ microspheres by using CeO₂ as cocatalyst, *Appl. Surf. Sci.* 464 (2019) 388–395.

[43] J. Zhang, Y. Hu, D. Liu, Y. Yu, B. Zhang, Enhancing oxygen evolution reaction at high current densities on amorphous-like Ni–Fe–S ultrathin nanosheets via oxygen incorporation and electrochemical tuning, *Adv. Sci.* 4 (2017), 1600343.

[44] X. Zu, Y. Zhao, X. Li, R. Chen, W. Shao, Z. Wang, J. Hu, J. Zhu, Y. Pan, Y. Sun, Y. Xie, Ultrastable and efficient visible-light-driven CO₂ reduction triggered by regenerative oxygen-vacancies in Bi₂O₂CO₃ nanosheets, *Angew. Chem. Int. Ed.* 60 (2021) 13840–13846.

[45] J. Wu, X. Li, W. Shi, P. Ling, Y. Sun, X. Jiao, S. Gao, L. Liang, J. Xu, W. Yan, C. Wang, Y. Xie, Efficient visible-light-driven CO₂ reduction mediated by defect-engineered BiOBr atomic layers, *Angew. Chem. Int. Ed.* 130 (2018) 8855–8859.

[46] X. Li, S. Wang, L. Li, Y. Sun, Y. Xie, Progress and perspective for in situ studies of CO₂ reduction, *J. Am. Chem. Soc.* 142 (2020) 9567–9581.

[47] G. Qian, W. Lyu, X. Zhao, J. Zhou, R. Fang, F. Wang, Y. Li, Efficient photoreduction of diluted CO₂ to tunable syngas by Ni–Co dual sites through d-band center manipulation, *Angew. Chem. Int. Ed.* 61 (2022), e202210576.

[48] Q. Li, S. Wang, Z. Sun, Q. Tang, Y. Liu, L. Wang, H. Wang, Z. Wu, Enhanced CH₄ selectivity in CO₂ photocatalytic reduction over carbon quantum dots decorated and oxygen doping g-C₃N₄, *Nano Res.* 12 (2019) 2749–2759.

[49] L. Cheng, X. Yue, L. Wang, D. Zhang, P. Zhang, J. Fan, Q. Xiang, Dual-single-atom tailoring with bifunctional integration for high-performance CO₂ photoreduction, *Adv. Mater.* 33 (2021), 2105135.

[50] A. Wang, S. Wu, J. Dong, R. Wang, J. Wang, J. Zhang, S. Zhong, S. Bai, Interfacial facet engineering on the Schottky barrier between plasmonic Au and TiO₂ in boosting the photocatalytic CO₂ reduction under ultraviolet and visible light irradiation, *Chem. Eng. J.* 404 (2021), 127145.

[51] S. Zhong, Y. Xi, Q. Chen, J. Chen, S. Bai, Bridge engineering in photocatalysis and photoelectrocatalysis, *Nanoscale* 12 (2020) 5764–5791.

[52] C.V. Reddy, I.N. Reddy, K.R. Reddy, S. Jaesool, K. Yoo, Template-free synthesis of tetragonal Co-doped ZrO₂ nanoparticles for applications in electrochemical energy storage and water treatment, *Electrochim. Acta* 317 (2019) 416–426.

[53] C.V. Reddy, I.N. Reddy, B. Akkinenpally, K.R. Reddy, J. Shim, Synthesis and photoelectrochemical water oxidation of (Y, Cu) codoped α -Fe₂O₃ nanostructure photoanode, *J. Alloy. Compd.* 814 (2020), 152349.

[54] T. Wu, E. Song, S. Zhang, M. Luo, C. Zhao, W. Zhao, J. Liu, F. Huang, Engineering metallic heterostructure based on Ni₃N and 2M-MoS₂ for alkaline water electrolysis with industry-compatible current density and stability, *Adv. Mater.* 34 (2022), 2108505.

[55] J. Theerthagiri, R. Sudha, K. Premnath, P. Arunachalam, J. Madhavan, A.M. Al-Mayouf, Growth of iron diselenide nanorods on graphene oxide nanosheets as advanced electrocatalyst for hydrogen evolution reaction, *Int. J. Hydrog. Energy* 42 (2017) 13020–13030.

[56] S. Liang, G. Zeng, X. Zhong, H. Deng, Z. Zhong, Z. Lin, J. Huang, Efficient photoreduction of diluted CO₂ using lattice-strained Ni_{1-x}Se nanoflowers, *J. CO₂ Util.* 64 (2022), 102193.

[57] X. Wu, W. Zhao, Y. Hu, G. Xiao, H. Ni, S. Ikeda, Y. Ng, F. Jiang, Research on the influence of the interfacial properties between a Cu₃BiS₃ film and an In_xCd_{1-x}S buffer layer for photoelectrochemical water splitting, *Adv. Sci.* 9 (2022), 2204029.

[58] S. Wang, W. Yao, J. Lin, Z. Ding, X. Wang, Cobalt imidazolate metal-organic frameworks photosplit CO₂ under mild reaction conditions, *Angew. Chem. Int. Ed.* 53 (2014) 1034–1038.

[59] X. Lin, Z. Xie, B. Su, M. Zheng, W. Dai, Y. Hou, Z. Ding, W. Lin, Y. Fang, S. Wang, Well-defined Co₉S₈ cages enable the separation of photoexcited charges to promote visible-light CO₂ reduction, *Nanoscale* 13 (2021) 18070–18076.

[60] B. Li, F. Wei, B. Su, Z. Guo, Z. Ding, M.-Q. Yang, S. Wang, Mesoporous cobalt tungstate nanoparticles for efficient and stable visible-light-driven photocatalytic CO₂ reduction, *Mater. Today Energy* 24 (2022), 100943.

[61] D. Sheberla, J.C. Bachman, J.S. Elias, C.-J. Sun, Y. Shao-Horn, M. Dincă, Conductive MOF electrodes for stable supercapacitors with high areal capacitance, *Nat. Mater.* 16 (2017) 220–224.